



**Spontaneous assembly of strong and conductive
graphene/polypyrrole hybrid aerogels for energy storage**

Journal:	<i>Nanoscale</i>
Manuscript ID:	NR-ART-06-2014-003322.R1
Article Type:	Paper
Date Submitted by the Author:	10-Aug-2014
Complete List of Authors:	Sun, Rui; Suzhou Institute of Nano-tech and Nano-bionics, Chen, Hongyuan; Suzhou Institute of Nano-tech and Nano-bionics, Chinese Academy of Sciences, Li, Qingwen; Suzhou institute of nanotech and nanobionics, Division of nanodevices and nanomaterials Song, Qijun; Jiangnan University, Zhang, Xuetong; Beijing Institute of Technology,

ARTICLE

Spontaneous assembly of strong and conductive graphene/polypyrrole hybrid aerogels for energy storage

Cite this: DOI: 10.1039/x0xx00000x

Rui Sun,^{a,b} Hongyuan Chen,^b Qingwen Li,^b Qijun Song^{*,a} and Xuotong Zhang^{*,b,c}Received 00th January 2014,
Accepted 00th January 2014

DOI: 10.1039/x0xx00000x

www.rsc.org/

Spontaneous assembly of nanoscale building blocks into three-dimensional (3D) frameworks is a vital strategy for practical application in environmental remediation, energy storage /conversion, sensing devices, etc. Herein we report an environmentally-friendly, low cost, and easy to scale-up route to synthesize reduced graphene oxide (rGO)-polypyrrole (PPy) hybrid aerogels by applying this novel spontaneous assembly method for the first time. The strong interaction between rGO and PPy, the reaction mechanism, the doping(/conducting) behaviour and the electrochemical energy storage of the resulting hybrid aerogels have been fully characterized via FTIR, Raman, TG, XRD, SEM, TEM, nitrogen sorption tests, CV, EIS, etc. The results show that, for the resulting hybrid aerogels, the existence of PPy can significantly enhance the electrochemical capacitance of the rGO aerogels, while the existence of the rGO sheets can greatly enhance the mechanical property of the PPy assemblies.

Introduction

Aerogels, three-dimensional (3D) porous architectures, can be synthesized from molecular precursors by sol-gel processing or assembling of nanoscale building blocks (e.g. nanoparticles, nanotubes, nanosheets, etc.) with subsequent replacing of the liquids in wet gels with air without collapsing the interconnected microstructure via supercritical fluid drying or freeze drying. Some unique characteristics such as extremely low densities, large open pores and high inner surface areas enable aerogels to be applied in the fields of energy storage/conversion,¹⁻⁴ catalysis,⁵⁻⁷ environmental remediation,⁸⁻¹¹ sensing devices,¹²⁻¹⁴ and so on. But no aerogels have been so far reported via spontaneous assembly of the starting materials in the absence of oxidants, reductants, high temperature, etc.

Among various nanoscale building blocks, graphene is one of the most attractive 2D ones due to its excellent electronic, mechanical, optical, large-specific-surface-area and biocompatible properties.^{15, 16} Thus, the studies on the assembly of graphene nanosheets into 3D hydrogel/aerogel have flourished for the time being.¹⁷⁻¹⁹ However, trenchant conditions, such as high temperature, high pressure and hazardous chemical agents, are generally involved during various process. Moreover, a major challenge in graphene-based aerogels is that graphene nanosheets easily form irreversible agglomerates or even graphitic stacking due to strong inter-layer π - π interaction and hydrophobic interaction. Consequently, the inherent properties of pristine graphene nanosheets cannot be exploited thoroughly and the aerogels usually exhibit inferior mechanical property, which inhibits the application of the graphene-based aerogel, for instance, energy storage and conversion. Although metal salts have been introduced into GO solution to prevent the

overlap of reduced graphene oxide (rGO) nanosheets and maximize the specific surface area, this strategy is not very desirable due to its fussy and expensive process.²⁰⁻²²

Pyrrole (Py) is a heterocyclic aromatic compound comprising a five-membered ring which is used as a monomer in polypyrrole (PPy) synthesis via chemical- or electro-polymerization. PPy has been widely explored for its good conductivity, facile synthesis, low cost, good stability and high redox pseudocapacitive charge storage.²³⁻²⁵ Therefore, PPy is considered as a desired mediator to construct 3D graphene based composites. Lee and co-workers have reported that graphene oxide (GO) can be reduced by Py and the oligomers of Py adsorbed on the graphene nanosheets by π - π interaction under the help of heat treatment.²⁶ Bai et al. has synthesized the graphene oxide/conducting polymer composite hydrogels using GO and Py monomer as the feedstock with ammonia persulfate as an oxidizing agent.²⁷ 3D graphene-PPy hydrogels have been created by one-step self-assembly process in the presence of Cu^{2+} , which helps the realization of the oxidation polymerization of Py meanwhile the newly generated Cu^+ ions synchronously reduced GO into graphene for accomplishing the construction of the composite hydrogel.²⁸ In addition, graphene-PPy foam synthesized via a multistep route through hydrolytic condensation (cross-linking), polymerization reactions and hydrothermal reduction of GO was reported by Liu and co-workers.²⁹ Recently, a new method was created that 3D porous PPy-G foam was prepared by hydrothermal reduction of GO aqueous dispersion with Py monomer and consequently in situ electro-polymerization of Py.^{24, 25} As a result, all these 3D graphene-PPy architectures were prepared through multistep routes and trenchant conditions generally employed in the process of synthesis, which was desirable for

neither scale-up nor energy conservation and environment protection.^{30,31}

Herein we have developed a spontaneous assembly method to construct rGO-PPy hybrid aerogel at room temperature, which is environmentally-friendly and easy to scale-up. The redox reaction between GO and Py has resulted in reduction of GO and polymerization of Py in the meantime without addition of any other oxidation or reduction agents. Various mass ratios of GO to Py have been studied for the formation of rGO-PPy hybrid hydrogels, and specific surface area, thermal stability, electrical conductivity and mechanical properties of the corresponding hybrid aerogels have also been studied. As a supercapacitor electrode material, the rGO-PPy aerogel has possessed high specific capacitance (304 F/g) at the current density of 0.5 A/g in an aqueous electrolyte. The work presented here, to the best of our knowledge, is the first report on the spontaneous assembly of the hybrid aerogels in the absence of any other oxidants as well as reductants with extremely mild conduction. Our work might also give inspiration to synthesize more hybrid aerogels based on graphene and any other conducting polymers such as polyaniline, polythiophene, etc., and the resulting hybrid aerogels might find broad application in the fields including energy storage, industrial catalysis, water purification, etc.

Experimental

Materials

Graphite (crystalline powder, 400 mesh), P₂O₅, K₂S₂O₇, 30% H₂O₂, HCl and H₂SO₄ were purchased from Sinopharm Chemical Reagent Company. These chemicals were in analytical grade and were used without further purification. Py monomer was purchased from Qiangsheng Chemical Reagent Company and was further purified by vacuum distillation and then stored at 0 °C before use. GO was prepared from graphite powder by a modified Hummers method reported in our previous study.³²

Synthesis of rGO-PPy hybrid hydrogels/aerogels

rGO-PPy hybrid hydrogels were synthesized via an in-situ polymerization method. Typically, different amount of purified Py was added into 4 mL 8 mg/mL GO suspension under stirring and dispersed by ultrasonication to obtain a homogenous solution. Then the reaction mixture was kept at ambient condition (~25 °C) for three days to obtain rGO-PPy hydrogel, which was defined as aging process. After aging, the hydrogel was washed with ethanol to remove impurities in the hydrogel network by the solvent-exchange process, then supercritical dried with CO₂ (40 °C, 10 MPa) for 12 hours to obtain rGO-PPy hybrid aerogel. To investigate the effect of synthetic conditions, the aerogels with initial mass ratios of GO to Py of 100:1, 50:1, 40:1, 30:1, 20:1, 15:1, 9:1, 7:1, 5:1, 3:1, 1:1, 1:3, 1:5, 1:7, 1:9, 1:10, 1:20 and 1:30 were synthesized, which named as GP100, GP50, GP40, GP30, GP20, GP15, GP9, GP7, GP5, GP3, GP1, PG3, PG5, PG7, PG9, PG10, PG20, PG30 respectively. For comparison, rGO aerogel reduced by L-ascorbic acid with initial GO concentration of 8 mg/mL and polypyrrole aerogel were also prepared by the method as reported in the reference.^{32,33}

Electrochemical investigation on the rGO-PPy hybrid aerogels

Electrochemical performances of the products were investigated in a three-electrode test system by using an electrochemical workstation (Chenhua, CHI 660D) with a platinum wire and a saturated calomel electrode (SCE) as the counter electrode and the reference electrode, respectively. 6 M KOH aqueous solution was used as electrolyte. The CV curves were scanned from 5 mV/s to 50 mV/s within -1~0 V potential. The galvanostatic charge-discharge tests were carried out at the current density of 0.5A/g, 1A/g, 2A/g, 5A/g, 10A/g, respectively. The EIS was recorded under the frequency range from 0.01Hz to 100 MHz. The work electrode was made by pressing the as-prepared rGO-PPy hybrid aerogel into Ni foam with the size of 1.5 mm × 1.5mm under a pressure of 5 MPa without addition of any binders and other conductive additives. The rGO and PPy aerogels electrodes were prepared by the same procedure.

Instrumentation

The FT-IR spectra were acquired by a Nicolet 6700 Fourier Transform Infrared Spectrometer (FT-IR, Nicolet 6700, Thermo Fisher Scientific). The specimens for FT-IR measurement were prepared by grinding the rGO-PPy aerogel and KBr together, and then compressed into thin pellets under 10 MPa. Raman spectra were recorded using a LabRAM HR Raman Spectrometer (LabRAM HR, Horiba-JY) fitted with a 632.8 nm laser. The crystal structure was characterized by X-ray diffraction (XRD, D8 Advance, Bruker AXS). Field emission scanning electron microscopy (FESEM, Hitachi S-4800), X-ray Energy Dispersive Spectrometer (EDS, Apollo 40SDD) and transmission electron microscope (TEM, Tecnai G2 F20 S-Twin) were used to investigate the morphology and microstructure of the samples. The pore structure of the samples was analyzed by Surface Area Analyzer (Micrometrics, ASAP 2020 HD88). Brunauer-Emmett-Teller (BET) method and Barrett-Joyner-Halenda (BJH) model were utilized to calculate the BET specific surface area (SSA) and the pore size distributions, respectively. Thermo gravimetric analysis (TGA) was performed on TG 209 F1 thermogravimetric analyser (NETZSCH, TG 209 F1 Iris). A heating rate was set to 10 °C/min under N₂ and the analytical temperature region was set from ambient temperature to 900 °C. The conductivity of rGO-PPy aerogels was evaluated by four point probe tester (Hengci, ST-2258A). Nano Indenter (Agilent Technologies, G200) was used to explore the mechanical property of rGO-PPy aerogels.

Results and discussion

The procedure for fabricating the rGO-PPy aerogels is illustrated in Fig. 1a. Two important steps is included, namely, the synthesis of rGO-PPy hydrogels, and subsequent supercritical CO₂ drying. The GO aqueous suspension (4 mL, 8 mg/mL) was mixed uniformly with different amount of Py monomer by ultra-sonication for about 10 min. Ambient temperature (~25 °C) aging was allowed to get rGO-PPy hydrogel. During the aging process, Py monomer reduced GO into rGO and itself was oxidized into PPy. Three days later, the rGO-PPy hydrogel was obtained and consequently washed with plenty of water to get rid of un-polymerized Py, followed by solvent-exchange with alcohol. Supercritical CO₂ drying of the hydrogel was the final step to acquire the corresponding rGO-PPy aerogel. The densities of obtained rGO-PPy aerogels were

in the range from 28 to 45 mg/cm³ (see Fig. S11a). To get rGO-PPy hydrogels, the optimal mass ratios of GO to Py monomer should be below 40:1 as shown in Fig. 1b and the stable rGO-PPy hydrogels evaluated by a tube inversion method were seldom observed if mass ratios were higher than 40:1. The above phenomenon has demonstrated that much less reductant, Py acting as, is needed to reduce GO and to induce the assembly of rGO to 3D network than L-ascorbic acid as the reductant.³¹ With Py amount increasing, the obtained rGO-PPy hydrogels shrank to some extent due to the higher degree of reduction of GO by excess Py monomer and some PPy with low polymerization degree would diffuse out of the network, which made the reaction solution become yellow (Fig. S11b).

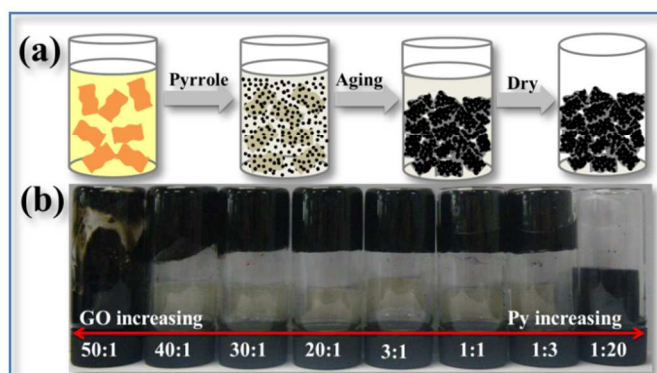


Fig. 1 (a) Schematic illustration of the formation mechanism of the rGO-PPy aerogels and (b) the effect of mass ratio of GO to Py on the hydrogel formation.

To understand the interactions between Py and GO, the FT-IR absorption spectra of PPy, GO, rGO and rGO-PPy aerogel (PG5) were acquired and compared as shown in Fig. 2a. For the curve of GO, the peaks located at 1735, 1043, 1226 and 1056 cm⁻¹ are corresponded to carbonyl C=O stretching vibration, carboxy C–O stretching vibration, C–OH stretching vibration, and epoxy C–O stretching vibration, respectively. The peak around 1616 cm⁻¹ can be assigned to the aromatic C=C stretching vibration.^{34–36} After chemical reduction (the curve of rGO), the peaks for oxygen-containing groups of GO are reduced significantly or entirely vanished. The remaining peaks at 1731, 1573 and 1222 cm⁻¹ are attributed to the carbonyl C=O, aromatic C=C and residual –OH. The results are in coincidence with a previous report.³⁷ The characteristic peaks of PPy locating at 1540 and 1450 cm⁻¹ are due to the symmetric and anti-symmetric ring-stretching modes, respectively. The bands at 1040 and 1300 cm⁻¹ are attributed to C–H band in-plane vibration and C–N stretching vibrations, respectively. Meanwhile, the peaks near 1170 and 893 cm⁻¹ indicate the doping state of PPy and the bands at 783 and 964 cm⁻¹ verify the presence of polymerized pyrrole.^{33, 37, 38} For the sample PG5, the above mentioned typical vibration band related to the oxygen-containing groups of the GO are reduced significantly or vanished and several new band located at 1562, 1461, 1041 and 1365 cm⁻¹ appear at the same time which are adhere to the stretching vibrations band of PPy rings and the C–N stretching vibration of Py, but shift a little bit to higher wavenumber direction, which probably due to the π - π interaction between rGO nanosheets and aromatic PPy rings. The peaks at 782 cm⁻¹ and 960 cm⁻¹ in the curve of PG5 are relatively weak, attributing to the low polymerization degree of PPy. In addition, the peaks relating to doping state of PPy in the

PG5 demonstrate that PPy is doped by protons dissociating from GO. These results indicate that GO nanosheets are reduced by Py and Py monomer is polymerized by the oxygen-containing groups of GO during the formation of the rGO-PPy hydrogels. However the doping level of PPy is limited due to the finite dissociation of carboxyl groups locating on the edges of GO nanosheets, which is corresponding to relatively low electrical conductivity of the rGO-PPy hybrid aerogels as shown in Fig. S12.

Raman spectroscopic measurements further confirm the polymerization of Py by GO nanosheets as shown in Fig. S13. The Raman spectrum of GO displays two bands located at 1353 cm⁻¹ and 1593 cm⁻¹. These two bands could be assigned to the D and G bands for carbon material. The D band corresponds to the first-order zone boundary phonons existing in defected graphene, whereas the G band corresponds to the in-plane bond-stretching motion of C-sp² atoms. The Raman spectrum of rGO aerogel reduced by L-ascorbic exhibits D and G band at 1324 and 1582 cm⁻¹ respectively. However, the intensity of the D band at 1324 cm⁻¹ increases obviously, which indicates that the significant decrease of the size of the in-plane sp² domains.^{39, 40} The Raman spectrum of PPy shows a band at around 1574 cm⁻¹, corresponding to the C=C backbone stretching of PPy. The band at 1326 cm⁻¹ is attributed to the ring stretching mode of PPy. The peak at 1043 cm⁻¹ is attributed to the C–H in-plane deformation. The bands located at about 983 and 933 cm⁻¹ correspond to ring deformations associated with the dication (bipolaron) and the radical cation (polaron), respectively.^{30, 35, 41, 42} The Raman spectrum of the PG5 aerogel shows the characteristic bands of PPy and an enhanced intensity of the band around 1330 cm⁻¹, which indicates strong interaction between PPy and rGO nanosheets.

The electronic structure and the surface chemistry composition of the as-prepared rGO-PPy aerogels were also investigated by XPS measurements. As shown in Fig. S14a, only the peaks corresponding to C1s (284.5 eV) and O1s (531.5 eV) signals can be clearly detected in the survey spectrum of the GO. It is worth noting that an additional signal centred at 399.5 eV ascribed to N1s can be observed for rGO-PPy aerogel (PG5), which is consistent with the EDX analysis mentioned above. Moreover, the O1s and C1s peaks of the carbons binding to oxygen atoms of PG5 become significantly weak and the C1s peak becomes much stronger in comparison with those of GO, which suggests that the recovery of π -conjugated structure. Fig. S14b shows the de-convolution C1s XPS spectrum of GO. Four types of carbon-containing functional groups centred at 284.5, 286.5, 287.3 and 288.7 eV, corresponding to C=C in aromatic rings, C–O (epoxy and alkoxy), C=O, and O–C=O (carboxyl) respectively, are detected.^{43–45} In the case of PG5 aerogel (Fig. S14c), the intensity of all C 1s peaks of carbons binding to oxygen, especially the peak of C–O (epoxy and alkoxy), decreases dramatically. At the same time, the C–N linkage peak (285.2 eV) can also be detected, which originates from PPy in PG5 aerogel.^{46, 47} In addition, a stronger π - π^* shake-up satellite peak around 291.5 eV, a characteristic of aromatic or conjugated systems,⁴⁸ is observed for PG5 rather than for GO, indicating that less defects in the structure are present in PG5 and the π - π interaction exhibits between rGO and PPy in PG5 aerogel. The peak centred about 399.5 eV corresponds to the N1s region. The symmetric N1s XPS peak of PG5 (Fig. S14d)

at 399.5 eV corresponds to “pyrrolic” nitrogen^{49, 50}, which is derived from PPy in PG5. The calculated atomic percentage of N in PG5 is 7.37 atom% (8.05 weight%), which is different from the original content of Py (PG5, the ratio of Py to GO is 5, which means the Py content in weight is 83.33% (N content in weight 17.41%)). The main reason of N content decreasing is that Py could not be totally polymerized in the reaction precession, which is in accordance with the results in Fig. S11b.

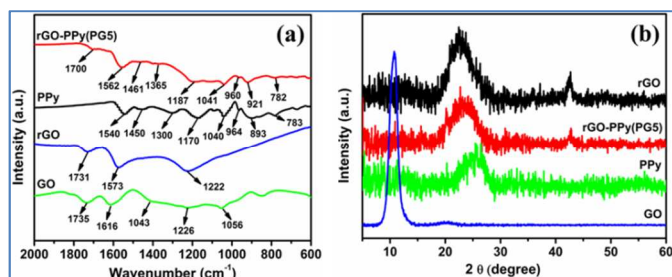


Fig. 2 (a) FT-IR spectra and (b) XRD patterns of GO, PPy, rGO-PPy and rGO reduced by L-ascorbic acid.

The XRD patterns reveal of crystal forms of pure PPy, GO, rGO-PPy aerogel (PG5) and rGO aerogel as shown in Fig. 2b. A broad characteristic peak of PPy appears at about 25°, indicating their amorphous nature.^{38, 51} The feature diffraction peak of GO centred at 10.7°, corresponding to the interlayer spacing of 0.77 nm. For rGO reduced by L-ascorbic acid, the diffraction peaks at 22.4° and 42.6° can be attributed to the graphite-like structure (002) and (100), respectively.⁵² In the case of PG5, the peak located at 10.7° disappears, which indicates the successful reduction of GO with Py acting as reductant. The peak at 23.1° can be attributed to the diffraction peak of either PPy or rGO. The interaction between PPy and rGO has induced the peak to shift from their primary options. The peak located at 42.6° seen in the rGO-PPy is a fingerprint peak for graphite, due to the (100) diffraction, indicating the reformation of graphitic microcrystals on the graphene plane due to the reduction of GO by Py monomer, which is accordance with the rGO aerogel reduced by L-ascorbic acid.

The field emission scanning electron microscope (FESEM) images manifest the microstructure of the rGO-PPy aerogels as shown in Fig 3a-b and Fig. S15. The rGO-PPy aerogel (PG5) has a microporous 3D network with interconnected pores with a wide size distribution due to randomly self-assembled inter-twisted rGO nanosheets. What's more, the solid walls of the pores are thin, which demonstrates that the stacking of rGO nanosheets is inhibited by PPy remarkably. The mesoporous nature of rGO-PPy aerogels is further investigated by the nitrogen physisorption measurement. The N₂ adsorption isotherms of rGO-PPy aerogel (GP3) (Fig. 3c) is of type IV attributing to monolayer-multilayer adsorption, suggesting the mesoporous nature of the rGO-PPy aerogel. The N₂ adsorption-desorption isotherm of rGO-PPy aerogel (GP3) exhibits hysteresis loop with the character of H4, indicating the presence of slit-like pores.⁵³ The hysteresis between the adsorption and desorption branches (at 0.4–0.6 P/P₀) further suggests a highly uniform pore size with no pore-blocking effects from narrow pores during desorption,⁵⁴ which conforms to the pore-size distribution plots calculated using the Barrett–Joyner–Halenda (BJH) method from the desorption branch of the isotherm. The pore size is mainly about 3.9 nm as shown in Fig. 3d. The Brunauer–Emmett–Teller (BET) analysis further reveals the

specific surface area of rGO-PPy aerogel (GP3) with the value of 408 m²/g. As comparison, rGO aerogel exhibits a similar adsorption-desorption isotherm but lower BET specific area (167 m²/g, Fig. S16), resulting from stacking and coalescing of rGO nanosheets. The energy dispersive X-ray (EDS) is employed to detect the distribution of PPy within the rGO-PPy aerogels. As shown in Fig. S17, carbon, nitrogen and oxygen element in the rGO-PPy aerogels distribute homogenously, indicating that the uniform distribution of PPy on rGO nanosheets.

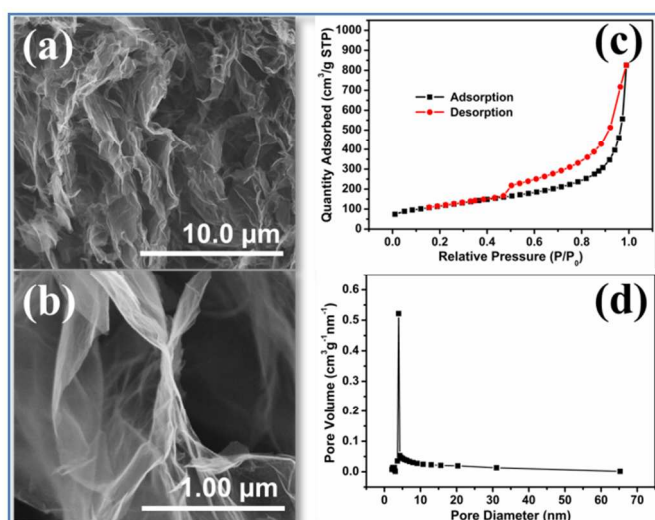


Fig. 3 (a-b) SEM images of rGO-PPy (PG5) aerogel with different magnifications; (c-d) Nitrogen adsorption-desorption isotherm of rGO-PPy (GP3) aerogel and the corresponding pore-size distributions.

The geometrical morphology of PPy is further displayed by TEM and HR-TEM images as shown in Fig. 4 (and Fig. S18). For GO nanosheets, leaf-like transparent sheets with wrinkles are observed in Fig. 4a. Furthermore, according to the HR-TEM results, cleanly plate can be seen in the Fig. 4b. The selected area electron diffraction (SAED) pattern (the inset of Fig. 4b) shows only diffraction rings, indicating the disordered nature of GO. As shown in the Fig 4c-d, PPy in the form of plate-like nanoparticles with different size disorderedly anchors on rGO nanosheets, which could ascribe to that the polymerization of Py via different oxygen-containing groups with different oxidizing ability randomly attached on GO nanosheets. The SAED of rGO-PPy aerogel (PG5) shows several bright spots and some amorphous circles, which are derived from rGO and amorphous PPy respectively. The comparison between GO and PG5 indicates that GO is reduced by Py and Py is polymerized by oxygen-containing groups of GO simultaneously. What is more, the geometrical morphology of PPy also proves that slit-like pores in the GP3 are constructed by plate-like PPy nanoparticles.

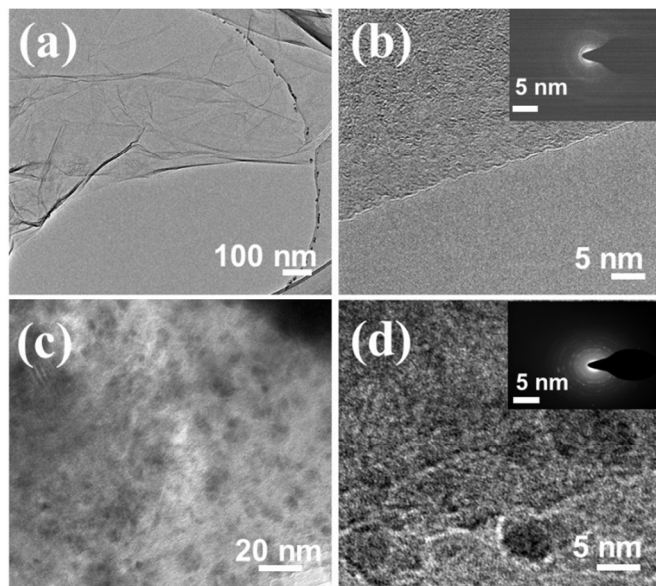


Fig. 4 TEM images of GO nanosheets (a,b) and the as-prepared rGO-PPy(PG5) aerogel (c,d) at different magnifications. Inserts are the respective SAED.

The thermal stabilities of GO, rGO, PPy and the rGO-PPy aerogel (PG5) are shown in Fig. 5a. It can be seen from this figure that all the products show different mass loss below 100 °C due to de-intercalation of water absorbed in the products. In the case of pure PPy, nearly 21.24% weight loss occurs at around 200 °C, ascribed to the decomposition of PPy chains.^{55, 56} 14.19% of its mass is maintained at 900 °C. As for GO, it displays a steep weight loss at around 189 °C, ascribed to the decomposition of labile oxygen-containing groups of GO, similar results were reported by Fang et al.⁵⁷ With the increment of temperature, the residual oxygen-containing groups with high bond energy decompose gradually. A 51.04% mass loss has been detected when the temperature rises to 900 °C. rGO shows a weight loss about 18.59% at 100–500 °C due to the removal of oxygen-containing groups by L-ascorbic acid, illustrating a much higher thermal stability in comparison with GO. The remaining small fraction of stable oxygen-containing groups on the rGO nanosheets is removed during the TG heating scan. 51.1% initial mass of rGO is reserved at 900 °C. The TG curve of PG5 is seriously different from pure GO and pure PPy. 23.84% of mass loss for PG5 at 100–500 °C replaces the steep weight loss of 38.14% for GO at the same temperature, which can be ascribed to that some oxygen-containing groups of GO are removed by Py. 59.13% of PG5 in weight is still remained at 900 °C, indicating that it is much more stable than the individual GO, PPy and even rGO aerogel reduced by L-ascorbic acid. The possible reasons for high thermal stability of PG5 are as follows. Firstly, most oxygen-containing groups of GO is removed by Py monomer and Py is oxidatively polymerized by GO simultaneously. Secondly, the sandwich-like structure of PG5 inhibits the thermal decomposition of rGO and PPy. Thirdly, the strong doping interaction between PPy and protons dissociating from rGO, which confirms from the FT-IR and Raman results, increases the energy for decomposing rGO and PPy.

The mechanical property of rGO-PPy aerogel (PG5) and rGO aerogel are investigated by nanoindentation test. Fig. 5b shows the storage modulus and loss modulus of PG5 aerogel

and rGO aerogel. For both PG5 and rGO aerogels, all the storage modulus values are higher than the loss modulus values over the entire range of frequencies, indicating that an elastic rather than viscous response of the composite aerogels under the small-deformation oscillation and that both rGO-PPy aerogel and rGO aerogel have permanent cross-linked network.^{32, 58, 59} The storage modulus of 12.2 MPa for PG5 aerogel is much higher than the value of 6.36 MPa for rGO aerogel, which manifest rGO-PPy aerogel exhibits better elastic response performance than rGO aerogel. On the other hand, the mechanical performance of PG5 is much more outstanding than that of other aerogels.^{60–62} This remarkable mechanical property of rGO-PPy aerogel can be attributed to the factors as follows: a) the strong π - π interaction between rGO nanosheets and PPy chains; b) PPy acting as cross-linker in the rGO-PPy aerogels with sandwich-like structure; c) the doping reaction between PPy chains and protons dissociated from rGO nanosheets; d) the excellent mechanical property of the rGO nanosheets themselves.

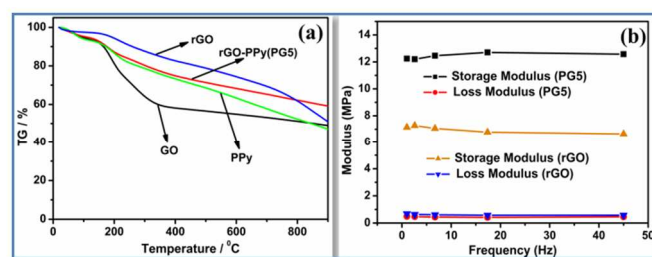


Fig. 5 (a) TG curves of GO, pure PPy, rGO-PPy (PG5) aerogel and rGO reduced by L-ascorbic; (b) Mechanical performance of rGO-PPy aerogel (PG5) and rGO aerogel.

The large BET surface areas and pore volumes, together with excellent mechanical properties, can make these rGO-PPy aerogels viable candidates for use in many fields such as energy storage, catalysis, sensors, etc. It can be seen that the CV curve of rGO aerogel (Fig. 6a) exhibits a typical rectangular shape, implying pure electrical double-layer capacitive behaviour. In contrast, the CV curve of GP3 aerogel displays a box-like shape combined with a pair of redox peaks in the potential range of -0.7~0.5 V. Fig. S19a shows the CV curves of GP3 aerogel, pure PPy and GO, there is no redox peaks in the potential range of -0.7~0.5 V for pure PPy and GO and the areas covered by the CV curves of pure PPy and GO are much smaller than that of GP3. The phenomenon above demonstrates that the redox peaks appearing in GP3 CV curves is caused by the PPy doped with proton dissociating from rGO and indicates the coexistence of both the electrical double-layer capacitance and pseudo-capacitance.^{63, 64} With the increase of the PPy content in rGO-PPy hybrid aerogels, the intensity of the redox peaks shows the tendency of monotonically increasing and decreasing in sequence and GP3 exhibits the highest redox peaks currents, which manifests that GP3 realizes the best synergistic effect between rGO and PPy. Fig. 6b shows the typical CV curves of the GP3 aerogel with various scan rates. With an increase in scan rate, the current response increases accordingly. The CV curves keep their shape with small distortions, which implies that the GP3 aerogel electrode has good rate performance and low internal resistance. Fig. S19b shows the galvanostatic charge-discharge curves of GP3, rGO, GO and pure PPy at the current density of 0.5 A/g. It

can be seen that GP3 aerogel exhibits nonsymmetric triangular shape, which is also the signal of the existence of pseudo-capacitance besides electric double layer capacitance. The specific capacitances calculated from the slope of the charge discharge curves is 304 F/g, 230.8 F/g at current density of 0.5 A/g and 1 A/g respectively, which is higher than the performance of supercapacitors made with graphene aerogels prepared by one-step hydrothermal processing⁶⁵ and by L-ascorbic acid reduction.⁶⁶ This electrochemical performance enhancement could be ascribed to two factors, namely, the redox peaks of PPy and the porous surface morphology of GP3 aerogel. In order to further investigate the synergistic effect between PPy and rGO, we evaluated the specific capacitances of rGO-PPy aerogels with different mass ratios of GO to Py and rGO as shown in Fig. 6c. The specific capacitances of all the samples decrease with the increase in the current density, which can attribute to the required time for ionic migration in the material. The specific capacitance of rGO aerogel is much lower than that of rGO-PPy aerogels at the same current density, which is attributed to that the self-aggregation of rGO in the reduction process makes the rGO aerogel provide less access for electrolyte. Increase in the specific surface area of the rGO-PPy hybrid aerogels in comparison with rGO aerogel is the main reason for the improved capacitance performance, which is consistent with the BET specific area evaluated above. Pseudo-capacitance donated by PPy in rGO-PPy aerogels also plays an important role in enhancing the performance of capacitance. For rGO-PPy aerogels, there is an initial increase in the values of the specific capacitance with an increase of Py amount added in the reaction mixture as shown in Table S11. GP3 aerogel shows the highest specific capacitance compared with other rGO-PPy aerogel electrodes, attributing to the best synergistic of rGO and PPy. The highest BET specific surface area and pseudo-capacitance donated by PPy result in the highest specific capacitance of GP3. Electrochemical impedance spectroscopy (EIS) analysis was carried out in a frequency range of 0.01-10 kHz to investigate the charge-transfer resistance and the ion diffusion rate of the obtained rGO-PPy aerogels and rGO aerogel as shown in Fig. 6d. These results provide important clues to understand the mechanism behind the different supercapacitive performance exhibited by the above aerogels. The Nyquist plots of all aerogels are composed of semicircles in the high frequency region and straight line in the low frequency region. The equivalent circuit model of all Nyquist plots exhibits that the whole capacitor circuit is constructed by R_s , R_{ct} , CPE and Z_w as shown in the insert of Fig. 6d. R_s is the internal resistance, representing the sum of the electrolyte solution resistance, the intrinsic resistance of active material and the contact resistance at the electrode-electrolyte interface, in which the electrolyte solution resistance is commonly predominant.⁴⁸ R_s in the Nyquist plot equals to the value of the intercept of the semicircle with X-axis. R_{ct} is charge-transfer resistance, which corresponding to the semicircular portion at the high frequency range. R_{ct} in the Nyquist is related to charge transfer through three electrode-electrolyte interface.⁶⁷ Z_w is the Warburg resistance related to the ion diffusion/transport in the electrolyte, which fits to the linear part in the mid-frequency region⁶⁸. A constant phase element used instead of pure capacitance due to the depressed semicircle. The results of fitting were shown in Fig. S110, which demonstrates the equivalent circuit model is reasonable. The Nyquist plot of

rGO aerogel shows a small semicircle in high frequency region and the value of R_s and R_{ct} of rGO electrode are 0.3362 Ω and 2.125 Ω respectively, which could ascribe to the little residual oxygen-containing groups. All of rGO-PPy samples exhibit obvious semicircle in the high frequency, demonstrating that rGO-PPy have larger interfacial charge-transfer resistance as compared to rGO aerogel. Calculated by using Zview software, the charge transfer resistance of GP3 is 7.814 Ω , which is smaller than 37.94 Ω of GP5, attributing to that GO is further reduced by Py. While the charge transfer resistance increases gradually with the increment of Py monomer which is further polymerized in the form of undoped state (as shown in Table S12). The lowest R_{ct} of GP3 could be explained by the synthetic mechanism of the rGO-PPy aerogels. The resistance of rGO-PPy aerogel is reduced by reducing GO to rGO though Py monomer, while the polymerization of Py to PPy induce the rise of the resistance for the rGO-PPy aerogel due to lack of further doping by protons. The rGO-PPy aerogel with the lowest resistance is prepared at the appropriate mass ratio of GO to Py that GO could be reduced by Py monomer and the polymerized PPy doped by proton anchored on rGO nano-sheet. The straight line in the high frequency of GP3 leans more towards imaginary axis than that of others, demonstrating that higher specific capacitance. To investigate the electrochemical stability of rGO-PPy aerogel, galvanostatic charge-discharge cycling was performed at a current density of 1 A/g (Fig. S111). GP3 shows an initial specific capacitance value of 230.8 F/g. At the initial charge-discharge cycling, the decrease of the specific capacitance is observed, resulting from the structure change of PPy such as decompose of PPy main chain during the repeated charge/discharge cycles in strong basic environment. After 50 cycles, the specific capacitance of GP3 drops down to 134 F/g, which is 58.26% of initial specific capacitance value. The decrease in GP3 capacitance could be ascribed to the decomposition of PPy chains with low degree of polymerization in the strong base environment. The retained capacitance is provided by rGO, thanks to its superior chemical and electrochemical stability. This indicates that Py is polymerized by oxygen-containing groups of GO and GO is reduced by Py at the same time, which is the key to synthesize rGO-PPy aerogels. The electrochemical measurements not only investigate the energy storage capabilities of rGO-PPy aerogels but also further illuminate the reaction mechanism between GO and Py monomer. We believe that the rGO-PPy aerogel based supercapacitor can be further optimized for the best performance by adjusting the synthetic parameters, annealing the resulting products, etc.

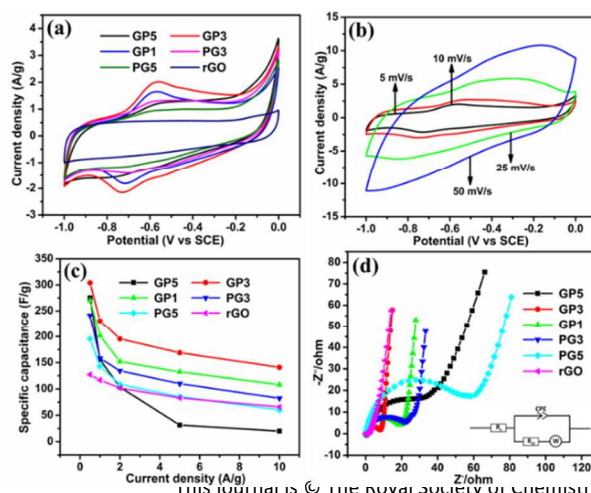


Fig.6 Electrochemical characterization of rGO-PPy aerogels electrodes. (a) CV curves (5 mV/s) of rGO-PPy aerogels and rGO aerogel, (b) CV curves of GP3 at different scan rates, (c) variation in the specific capacitance of rGO-PPy aerogels and rGO aerogel as a function of current density, (d) Nyquist plots of rGO-PPy aerogels and rGO aerogel (the insert is the equivalent circuit model of Nyquist plots)

Conclusions

rGO-PPy hybrid aerogels have been prepared through an in-situ redox polymerization (i.e., spontaneous assembly) method without adding any other reductants or oxidizing agents. The obtained hybrid aerogels have exhibited excellent mechanical property and outstanding electrochemical supercapacitor performance, considerably higher than rGO counterpart reduced by L-ascorbic acid. High mechanical property is ascribed to the strong π - π interaction between PPy and rGO and the doping reaction of the protons dissociated from rGO into PPy main chain. The method might pave the way to prepare various rGO-conducting polymer hybrid aerogels with potential application in many fields.

Acknowledgements

This work was financially supported by the National Natural Science Foundation of China (21373024), the 100 Talents Program of the Chinese Academy of Science, and the Innovation Program of the Beijing Institute of Technology.

Notes and references

^aSchool of Chemical and Material Engineering, Jiangnan University, Wuxi, 214122, P. R. China. E-mail: qsong@jiangnan.edu.cn

^bSuzhou Institute of Nano-tech & Nano-bionics, Chinese Academy of Sciences, Suzhou, 215123, P. R. China; Tel: 0512-62872821; Email: zhangxtchina@yahoo.com.

^cSchool of Materials Science & Engineering, Beijing Institute of Technology, Beijing, 100081, P. R. China.

†Electronic Supplementary Information (ESI) available: Fig. S11-Fig. S111 and Table S11-S12 including conductivity, density data and Raman spectra, etc. See DOI: 10.1039/b000000x/

- Z. S. Wu, A. Winter, L. Chen, Y. Sun, A. Turchanin, X. Feng and K. Müllen, *Advanced Materials*, 2012, **24**, 5130-5135.
- J. Lin, C. Zhang, Z. Yan, Y. Zhu, Z. Peng, R. H. Hauge, D. Natelson and J. M. Tour, *Nano letters*, 2012, **13**, 72-78.
- L. Ren, K. Hui and K. Hui, *Journal of Materials Chemistry A*, 2013, **1**, 5689-5694.
- W. Chen, S. Li, C. Chen and L. Yan, *Advanced Materials*, 2011, **23**, 5679-5683.
- T. Wu, M. Chen, L. Zhang, X. Xu, Y. Liu, J. Yan, W. Wang and J. Gao, *Journal of Materials Chemistry A*, 2013, **1**, 7612-7621.
- C. Zhu and S. Dong, *Nanoscale*, 2013, **5**, 1753-1767.
- Z.-S. Wu, S. Yang, Y. Sun, K. Parvez, X. Feng and K. Müllen, *Journal of the American Chemical Society*, 2012, **134**, 9082-9085.
- H. Bi, Z. Yin, X. Cao, X. Xie, C. Tan, X. Huang, B. Chen, F. Chen, Q. Yang and X. Bu, *Advanced Materials*, 2013, **25**, 5916-5921.
- Z. Niu, J. Chen, H. H. Hng, J. Ma and X. Chen, *Advanced Materials*, 2012, **24**, 4144-4150.
- H. Bi, X. Huang, X. Wu, X. Cao, C. Tan, Z. Yin, X. Lu, L. Sun and H. Zhang, *Small*, 2014.
- J. G. Duque, C. E. Hamilton, G. Gupta, S. A. Crooker, J. J. Crochet, A. Mohite, H. Htoon, K. A. D. Obrey, A. M. Dattelbaum and S. K. Doorn, *ACS nano*, 2011, **5**, 6686-6694.
- F. Yavari, Z. Chen, A. V. Thomas, W. Ren, H.-M. Cheng and N. Koratkar, *Scientific reports*, 2011, **1**.
- S. R. Ng, C. X. Guo and C. M. Li, *Electroanalysis*, 2011, **23**, 442-448.
- X. Dong, Y. Ma, G. Zhu, Y. Huang, J. Wang, M. B. Chan-Park, L. Wang, W. Huang and P. Chen, *J. Mater. Chem.*, 2012, **22**, 17044-17048.
- A. A. Balandin, S. Ghosh, W. Bao, I. Calizo, D. Teweldebrhan, F. Miao and C. N. Lau, *Nano letters*, 2008, **8**, 902-907.
- X. Wang, L. Zhi and K. Müllen, *Nano letters*, 2008, **8**, 323-327.
- Z. Sui, Q. Meng, X. Zhang, R. Ma and B. Cao, *Journal of Materials Chemistry*, 2012, **22**, 8767-8771.
- H. Yin, C. Zhang, F. Liu and Y. Hou, *Advanced Functional Materials*, 2014.
- L. Xiao, D. Wu, S. Han, Y. Huang, S. Li, M. He, F. Zhang and X. Feng, *ACS applied materials & interfaces*, 2013, **5**, 3764-3769.
- Z.-S. Wu, W. Ren, L. Wen, L. Gao, J. Zhao, Z. Chen, G. Zhou, F. Li and H.-M. Cheng, *ACS nano*, 2010, **4**, 3187-3194.
- Y. He, W. Chen, X. Li, Z. Zhang, J. Fu, C. Zhao and E. Xie, *ACS nano*, 2012, **7**, 174-182.
- L. Shen, X. Zhang, H. Li, C. Yuan and G. Cao, *The Journal of Physical Chemistry Letters*, 2011, **2**, 3096-3101.
- R. Sharma, A. Rastogi and S. Desu, *Electrochemistry Communications*, 2008, **10**, 268-272.
- A. Liu, C. Li, H. Bai and G. Shi, *The Journal of Physical Chemistry C*, 2010, **114**, 22783-22789.
- J. Zhang, P. Chen, B. H. Oh and M. B. Chan-Park, *Nanoscale*, 2013, **5**, 9860-9866.
- C. A. Amarnath, C. E. Hong, N. H. Kim, B.-C. Ku, T. Kuila and J. H. Lee, *Carbon*, 2011, **49**, 3497-3502.
- H. Bai, K. Sheng, P. Zhang, C. Li and G. Shi, *J. Mater. Chem.*, 2011, **21**, 18653-18658.
- H. Zhou, T. Ni, X. Qing, X. Yue, G. Li and Y. Lu, *RSC Advances*, 2014, **4**, 4134-4139.
- H. Li, L. Liu and F. Yang, *Journal of Materials Chemistry A*, 2013, **1**, 3446-3453.
- (a) J. Liu, Z. Wang, Y. Zhao, H. Cheng, C. Hu, L. Jiang and L. Qu, *Nanoscale*, 2012, **4**, 7563-7568. (b) S. Ye and J. Feng, *ACS Appl. Mater. Interfaces*, 2014, **6**, 9671-9679
- Y. Zhao, J. Liu, Y. Hu, H. Cheng, C. Hu, C. Jiang, L. Jiang, A. Cao and L. Qu, *Advanced Materials*, 2013, **25**, 591-595.
- Z. Sui, X. Zhang, Y. Lei and Y. Luo, *Carbon*, 2011, **49**, 4314-4321.
- R. Temmer, R. Kiefer, A. Aabloo and T. Tamm, *Journal of Materials Chemistry A*, 2013, **1**, 15216-15219.
- Y. Si and E. T. Samulski, *Nano Letters*, 2008, **8**, 1679-1682.
- J. Liu, C. Chen, C. He, J. Zhao, X. Yang and H. Wang, *ACS nano*, 2012, **6**, 8194-8202.
- H. Zhang, T. Kuila, N. H. Kim, D. S. Yu and J. H. Lee, *Carbon*, 2014, **69**, 66-78.
- F. Gong, X. Xu, G. Zhou and Z.-S. Wang, *Physical Chemistry Chemical Physics*, 2013, **15**, 546-552.
- C. Bora and S. Dolui, *Polymer*, 2012, **53**, 923-932.
- S. Stankovich, D. A. Dikin, R. D. Piner, K. A. Kohlhaas, A. Kleinhammes, Y. Jia, Y. Wu, S. T. Nguyen and R. S. Ruoff, *Carbon*,

- 2007, 45, 1558-1565.
- 40 K. N. Kudin, B. Ozbas, H. C. Schniepp, R. K. Prud'Homme, I. A. Aksay and R. Car, *Nano letters*, 2008, 8, 36-41.
- 41 L. Mao, H. S. O. Chan and J. Wu, *RSC Advances*, 2012, 2, 10610-10617.
- 42 D. Zhang, X. Zhang, Y. Chen, P. Yu, C. Wang and Y. Ma, *Journal of Power Sources*, 2011, 196, 5990-5996.
- 43 U. N. Maiti, J. Lim, K. E. Lee, W. J. Lee and S. O. Kim, *Advanced Materials*, 2014, 26, 615-619.
- 44 Z. Sui, Q. Meng, X. Zhang, R. Ma and B. Cao, *Journal of Materials Chemistry*, 2012, 22, 8767-8771.
- 45 R. Li, C. Chen, J. Li, L. Xu, G. Xiao and D. Yan, *Journal of Materials Chemistry A*, 2014, 2, 3057-3064.
- 46 D. Wang, Y. Min, Y. Yu and B. Peng, *Journal of Colloid and Interface Science*, 2014, 417, 270-277.
- 47 L. Chen, X. Wang, X. Zhang and H. Zhang, *Journal of Materials Chemistry*, 2012, 22, 22090-22096.
- 48 B. Xu, S. Yue, Z. Sui, X. Zhang, S. Hou, G. Cao and Y. Yang, *Energy & Environmental Science*, 2011, 4, 2826-2830.
- 49 H. Chang, J. Kang, L. Chen, J. Wang, K. Ohmura, N. Chen, T. Fujita, H. Wu and M. Chen, *Nanoscale*, 2014, 6, 5960-5966.
- 50 R. Imran Jafri, N. Rajalakshmi and S. Ramaprabhu, *Journal of Materials Chemistry*, 2010, 20, 7114-7117.
- 51 H. Bai, K. Sheng, P. Zhang, C. Li and G. Shi, *Journal of Materials Chemistry*, 2011, 21, 18653-18658.
- 52 W. Chen and L. Yan, *Nanoscale*, 2011, 3, 3132-3137.
- 53 K. Sing, K. Sing, D. Everett, R. Haul, L. Moscou, R. Pierotti, J. Rouquerol and T. Siemieniowska, *Pure Appl. Chem*, 1982, 54, 2201.
- 54 S. Yang, X. Feng, L. Wang, K. Tang, J. Maier and K. Müllen, *Angewandte Chemie International Edition*, 2010, 49, 4795-4799.
- 55 J. Thieblemont, A. Brun, J. Marty, M. Planche and P. Calo, *Polymer*, 1995, 36, 1605-1610.
- 56 Y. Fan, Y. Liu, Q. Cai, Y. Liu and J. Zhang, *Synthetic Metals*, 2012, 162, 1815-1821.
- 57 M. Fang, K. Wang, H. Lu, Y. Yang and S. Nutt, *Journal of Materials Chemistry*, 2009, 19, 7098-7105.
- 58 J. H. Lee, J. Ahn, M. Masuda, J. Jaworski and J. H. Jung, *Langmuir*, 2013, 29, 13535-13541.
- 59 H.-P. Cong, X.-C. Ren, P. Wang and S.-H. Yu, *Acs Nano*, 2012, 6, 2693-2703.
- 60 S. Ye, J. Feng and P. Wu, *Journal of Materials Chemistry A*, 2013, 1, 3495-3502.
- 61 M. A. Worsley, S. O. Kucheyev, H. E. Mason, M. D. Merrill, B. P. Mayer, J. Lewicki, C. A. Valdez, M. E. Suss, M. Stadermann and P. J. Pauzauskie, *Chem. Commun.*, 2012, 48, 8428-8430.
- 62 Z. Han, Z. Tang, P. Li, G. Yang, Q. Zheng and J. Yang, *Nanoscale*, 2013, 5, 5462-5467.
- 63 B. Kim, J. Ko and G. Wallace, *Journal of Power Sources*, 2008, 177, 665-668.
- 64 J.-H. Kim, Y.-S. Lee, A. K. Sharma and C. G. Liu, *Electrochimica Acta*, 2006, 52, 1727-1732.
- 65 Y. Xu, K. Sheng, C. Li and G. Shi, *ACS nano*, 2010, 4, 4324-4330.
- 66 X. Zhang, Z. Sui, B. Xu, S. Yue, Y. Luo, W. Zhan and B. Liu, *Journal of Materials Chemistry*, 2011, 21, 6494-6497.
- 67 C. Xiang, M. Li, M. Zhi, A. Manivannan and N. Wu, *Journal of Materials Chemistry*, 2012, 22, 19161-19167.
- 68 D. Chen, L. Tang and J. Li, *Chemical Society Reviews*, 2010, 39, 3157-3180.